CALPHAD: Computer Coupling of Phase Diagrams and Thermochemistry 88 (2025) 102790

Contents lists available at ScienceDirect

Calphad

journal homepage: www.elsevier.com/locate/calphad

Experimental determination of AlN in microalloyed steel and thermodynamic analysis

Markus Führer [a,*], Sabine Zamberger [b], Erwin Povoden-Karadeniz [a,c]

[a] Christian Doppler Laboratory for Interfaces and Precipitation Engineering CDL IPE, Institute of Materials Science and Technology, TU Wien, Getreidemarkt 9, 1060, Vienna, Austria
[b] voestalpine Forschungsservicegesellschaft Donawitz GmbH, Kerpelystraße 199, 8700, Leoben, Austria
[c] Institute of Materials Science and Technology, TU Wien, Getreidemarkt 9, 1060, Vienna, Austria

ARTICLE INFO

Handling Editor: Prof. Z.K. Liu

Keywords:
Calphad
Thermodynamic stability
Particle analysis

ABSTRACT

Differential Scanning Calorimetry measurements are performed with a subsequent postprocessing routine specially designed for dilute systems, aiming at the evaluation of the solvus temperature of AlN in seven microalloyed steel laboratory melts. Computer-aided EDS particle analysis of the steel microstructure confirms the DSC results. With this consistent set of new data directly related to observed AlN stability, coupled with critically assessed thermodynamic data from the literature, the thermodynamic description of the AlN phase is reconsidered.

1. Introduction

For a long time within the steel production process, aluminum was mainly employed for deoxidation until the crucial importance of AlN precipitates for many steel properties was identified. Al microalloying additions can improve hot ductility, impact toughness, or weldability. AlN can avoid austenite grain coarsening due to the pinning of the grain boundaries [1], whereas excessive primary AlN can cause embrittlement [2,3]. The optimization of processing and properties of microalloyed steel thus demands accurate knowledge of the thermodynamic stability of AlN [4].

AlN is a stochiometric phase [5] with a hexagonal wurtzite structure, space group $P6_3mc$. On cooling, it starts to become stable in the austenite (γ) region of microalloyed steel, predominantly nucleating heterogeneously at grain boundaries [3] due to a high volumetric misfit beyond 70 % between the γ-matrix and AlN-precipitate [3,6,7]. However, in ferrite (α) in dependence on the nominal Al and N contents and the thermomechanical processing route [3,8–10], initially, metastable cubic rock-salt structured AlN with a size of 5–10 nm can form, which are subsequently converted into the stable hexagonal AlN modification [11].

Thermodynamic Calphad databases are designed by coupling binary and ternary subsystem descriptions, typically assessing a wide range of compositions but often not focusing on a particular composition space corner. This can lead to considerable deviations between the predicted and observed phase stabilities in low-alloyed materials [12]. Especially in steel, correctly describing the dilute corners is of special relevance because the typically occurring phase fractions range down to only some tenth of parts per million (ppm) [13]. To confirm the applicability of a database in microalloyed steel, the experimental input dataset must be extended to the dilute alloy composition range. In fact, in the case of the stability of AlN in steel, on the one hand, various, however in part deviating, proposals on the solubility products have been given [14–21]. On the other hand, microanalytic investigations of AlN are missing, obviously due to the difficulty of observation and thus lack of statistics with conventional methods. The low phase fraction and small diameter of AlN, combined with the relatively scattered, heterogeneous particle distribution, prevent the successful employment of conventional micro-characterization techniques. Thus, the occurrence of AlN has previously been confirmed indirectly, such as by metal-nitride gas equilibration [22,23] or by chemically dissolving the matrix and separating the precipitates using the Beeghly method [24]. Considering these limitations in the past, Calphad modeling of AlN for applications in dilute steel lacks robust and direct experimental input data.

In the present study, the employment of more recently presented methods [25,26] makes it realizable to precisely define chemical steel compositions, analyze more accurately the solvus temperature of the AlN precipitates in dilute microalloyed steel [26,27], and directly

---

* Corresponding author.
E-mail addresses: markus.fuehrer@tuwien.ac.at, fuehrer.markus@gmail.com (M. Führer).

https://doi.org/10.1016/j.calphad.2024.102790
Received 16 September 2024; Received in revised form 27 November 2024; Accepted 3 December 2024

observe AlN in the microstructure with sufficient statistics to compare the AlN stability as a function of different alloying [28]. The solvus temperature T_{solvus} of AlN is essential since it represents the maximum temperature for the occurrence of AlN in the microstructure. To the author's knowledge, the solvus temperature of AlN as a function of Al alloying has not been studied directly, i.e., coupling the thermodynamic endothermal signal at the AlN dissolution temperature to the microstructurally observed disappearance of the phase.

In this work, we reassess the Fe-rich corner of the system Fe-Al-N-C within the open-license MatCalc steel database mc_fe_v2.061 [29] based on new experimental data, focusing on the physically appropriate description of the phase stability of AlN. For this purpose, an assessment of available enthalpies of AlN formation [30–36] is combined with its solvus temperature as a function of Al alloying, which is determined with Differential Scanning Calorimetry (DSC) by the change of excess specific heat capacity C_p of the studied microalloyed steel due to the dissolution of AlN in austenite. The solvus temperature is confirmed by microstructural particle analysis with a high statistical significance. We use a computer-aided Energy Dispersive Spectroscopy (EDS) particle analysis method (PA) to cope with the difficult issue of precipitates being small and few in number. By combining the available experimental thermodynamic data for the enthalpy, entropy, and heat capacity of AlN with the measured solubility limits, it is possible to predict the AlN precipitation in dilute systems accurately. The developed multi-component database ME-Fe_CDLIPE2.0.1 is confidential, and its use is restricted to our industrial partners; thus, it is not presented here. However, Calphad parameters of the discussed phases fcc, bcc, MnS, and AlN within the system Fe-Al-Mn-S-N-C are inserted as supplementary data.

Mn is a minor alloying element in the studied steel, comprising around 0.1 to 0.25 wt% (see Table 3). Due to its high affinity to sulfur, Mn is added to avoid the possible adverse effects of sulfur on steel toughness [37]. Whereas Mn does not dissolve in AlN and does not influence the thermodynamic stability of the latter, several authors [14,38,39] reported a co-precipitation of AlN and MnS, with MnS acting as potential nucleation sites for AlN and thus significantly influencing the kinetics of AlN precipitation. The heterogeneous nucleation of AlN on the surface of MnS [55] is beneficial for AlN precipitation within a microstructure, where the precipitation of isolated AlN would otherwise not occur [38].

2. Critical literature survey on the thermodynamic properties, stability data, and calphad assessments of AlN

For the description of the stability of AlN precipitates in steel, often solubility products alone, in the form log(K) versus T, where K=(wt.%Al · wt.%N), are preferred over assessed values in thermodynamic databases. Costa e Silva [40,41] noted the discrepancies between these two data sets. Here, we aim to find the least squares of errors between experimental data and prediction by combining all critically reviewed available input data sets for a Calphad assessment, including enthalpies, heat capacities, derived entropies, solubility products, and DSC data. The following chapters, 2.1 to 2.4, critically discuss the different data groups that act as input data for the Calphad parametrization of the molar Gibbs energy polynomial of AlN. This sets the base for appropriate Calphad input data weighing, as described in Chapter 5.3.

2.1. Enthalpy of AlN formation

Table 1 lists the available standard heat of formation per mole of formula units at 298.15 K for AlN, $\Delta^{\circ}H_{AlN}$. The experimental values for $\Delta^{\circ}H_{AlN}$ lie within a relatively close range between −311.1 and −319.9 kJmol^{-1}, except for the data of −299.0 kJmol^{-1} resulting from combustion calorimetry [42]. This may be related to overlooked problems of incomplete combustion. The differences in the experimental heat of formation are attributed to individual inaccuracies associated with the different techniques, and it is not possible to refer to one of the investigation techniques as the most precise among the different sources [31–34]. In torsion effusion cell, the requirement of the calculation of the evaporation coefficient, and the derived equilibrium gas pressure are subject to some uncertainty within the method. Moreover, differences in the experimental heat of formation are attributed to impurity contents like Al_2O_3, which cannot be oxidized or nitrided [30]. Standard state data are extrapolated from high-T experiments by the thermodynamic second-law method.

Table 1
Standard heat of formation of AlN and the underlying technique.

Nr.	ΔH_f°(kJ/mol)	Technique	Ref.
1	−311.1 ± 4.3	High-temperature oxidative drop solution	[33]
2	−313.0 ± 4.8	Torsion effusion cell	[31]
3	−316.3 ± 1.7	Oxidation combustion calorimetry	[32]
4	−319.9 ± 0.8	Direct nitridation calorimetry	[34]
5	−299.0 ± 0.7	Combustion calorimetry	[42]
6	−312.5	Calculated from equilibrium data	[43]
7	−316.3	tabulated	[44]
8	−318.0	tabulated	[45,46]
9	−318.4 ± 2.1	tabulated	[47–49]
10	−318.0	Review, NIST-JANAF	[50]
11	−332.7	DFT, local density approximation (LDA)	[35]
12	−287.0	DFT, generalized gradient approximation (GGA)	[35]
13	−286.6	DFT, generalized gradient approximation (GGA)	[36]

The ab initio values, numbers 11 to 13 in Table 1, for the heat of formation of AlN show a wider spread and lie between −332.7 and −286.6 kJmol^{-1}, whereby according to Refs. [51,52] generalized gradient approximation (GGA) and local density approximation (LDA) likely suggest too high and too low enthalpies, respectively. This is related to the computed lattice parameters. An overestimated lattice parameter by GGA leads to lower binding forces and, thus, less negative enthalpies, and vice versa for LDA.

2.2. Molar entropy and heat capacity of AlN

Mah et al. [32], Sedmidubský et al. [53], and Chase [50] suggest for the standard molar entropy $S_{298.15}$ values of 20.08 Jmol^{-1}K^{-1}, 20.69 Jmol^{-1}K^{-1}, and 20.14 Jmol^{-1}K^{-1} respectively. For the heat capacity, consistent C_p of AlN at 298.15 K, values of 30.1248 JK^{-1} [32] and 29.866 JK^{-1} [53] are published.

2.3. Solubility products of AlN in austenite

The solubility product K defines the concentration product between Al and N in wt.%, where AlN is dissolved in the steel matrix at a specific temperature. Solubility products are then plotted logarithmic, log(K), as a function of temperature. The lower the log(K), the lower the respective concentrations of Al and N at which all AlN is dissolved. Opposite, AlN precipitation occurs at higher concentrations of Al and N than given by K. It is self-speaking that the log(K) is thus typically lower at lower temperatures: The phase boundary between steel matrix phase and precipitate at low temperatures is usually at more dilute compositions than at higher temperatures.

A large number of experimental data on the solubility of AlN in austenite is available, as shown in Fig. 1 and Table 2. It can be seen that there is a large scatter between the different proposals for solubility products. This can be related to the limitations of the different experimental quantification methods of the dissolution temperature for AlN, the chemical and technical accuracy limitations of the experimental method, and impurity issues [2]. Moreover, the formation of AlN can be influenced by the grain size [3] or heat treatment parameters [17], which are further possible contributions to the significant variation in literature data [2].

Most of the existing literature data for the solubility products shown in Table 2 were generated several decades ago when equilibrium N and

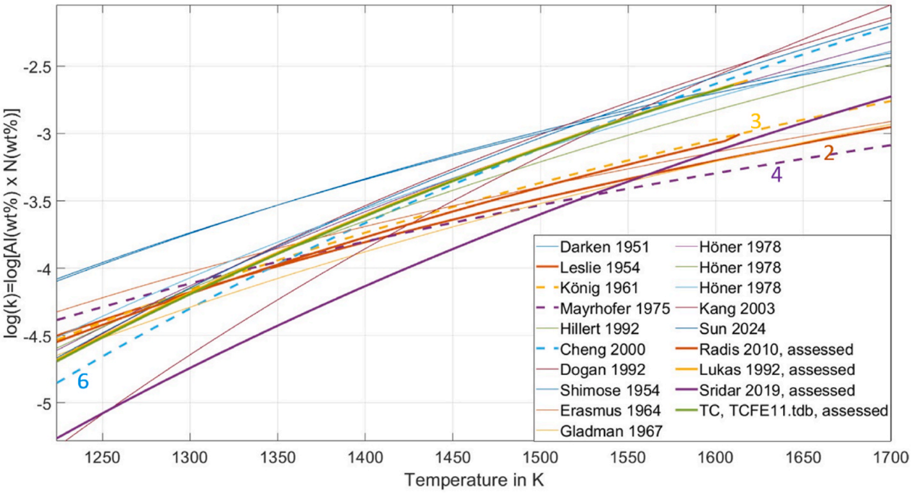

Fig. 1. Comparison of solubility products $\log(K) = \log[Al(\text{wt.\%}) \cdot N(\text{wt.\%})]$ in austenite from literature, see Table 2, and from thermodynamic descriptions, see chapter 2.4. The dotted lines are the most reliable descriptions following Gladman and Wilson [3] (Nr.2) and Radis et al. [2] (Numbers 3,4,6). The numbers in the plot correspond to Table 2. The expression 'assessed' in the legend accounts for evaluating the solubility product via fundamental thermodynamic calculations.

Table 2
Solubility products of aluminum nitride in austenite.

Nr.	$\text{Log}[Al(\text{wt.\%} \cdot N(\text{wt.\%}))]$	Method	Ref.
1	$1.95–7400/T$	Beeghly method	[15]
2	$1.03–6770/T$	Beeghly method	[19]
3	$1.8–7750/T$	Beeghly method	[18]
4	$0.18–5675/T + 2.4 \cdot Al(\text{wt.\%})$	Beeghly method	[20]
5	$4.382–11085/T$	Thermodynamic calculation	[16]
6	$4.599–11568/T$	Thermodynamic calculation	[14]
7	$0.528–5938/T$	Beeghly method	[64]
8	$1.790–7184/T$	Beeghly method	[65]
9	$0.725–6180/T$	Beeghly method	[62]
10	$1.480–7500/T$	Beeghly method	[66]
11	$3.577–10020/T$	Beeghly method	[67]
12	$2.923–9200/T$	Beeghly method	[67]
13	$3.079–9295/T$	Beeghly method	[67]
14	$6.40–14356/T$	Thermodynamic calculation	[59]
15	$-2.770 - 4772.35/T$	EDS particle analysis	[21]
16	$2.600–9710/T$	TEP [68]	[56]
17	$4.21–10863/T$	Thermodynamic calculation	[61]

Table 3
Composition of the vacuum induction melted alloys (wt.%).

Alloy	mass fraction in %						
	C	Al	N	Mn	S	O	Ti
Al1N65	0.517	0.009	0.0065	0.121	0.0060	0.0009	0.0002
Al4N78	0.520	0.038	0.0078	0.121	0.0063	0.0008	0.0002
Al7N88	0.513	0.070	0.0088	0.122	0.0061	0.0010	0.0002
Al12N86	0.518	0.119	0.0086	0.121	0.0057	0.0009	0.0003
Al3N63	0.492	0.029	0.0063	0.207	0.0061	0.0007	0.0005
Al6N59	0.493	0.060	0.0059	0.221	0.0063	0.0008	0.0005
Al12N65	0.494	0.115	0.0065	0.241	0.0064	0.0009	0.0007

Al contents were determined experimentally using the Beeghly method [24]. This method separates precipitates from the matrix by dissolving the matrix chemically, separating the precipitates physically, and determining their amount volumetrically or photometrically [54]. Major disadvantages of the Beeghly method [24], which are likely the main reasons for deviating results among different groups, are that it is not possible to extract very fine AlN particles due to limitations in the filtering step [3,41] and to distinguish them from any other co-extracted nitride [3,19,20,54]. Wilson and Gladman [3] state the threshold particle detection size of the Beeghly [24] method to be at about 10 nm. Only one study by Jeanmaire et al. [20] employs electron microscopy for the direct, quantitative determination of AlN in a high-strength X23NiCoCrMoAl13-6-3 maraging steel. Zheng et al. [21] then suggested the solubility product of AlN by using the measured area fraction of AlN by Jeanmaire et al. [55].

Such data connections between different groups are indeed also prone to errors within the evaluation. Siyasiya et al. [56] measured the variation of thermoelectric power (TEP [57]) of their specimens, brought it into relation with the effect of AlN precipitation, and evaluated a solubility product of AlN. TEP provides information on the amount of free interstitials in solid solution, which makes it possible to determine the precipitated fraction of nitrides. However, the resulting solubility product evaluated by TEP (Nr. 16 in Table 2) differs considerably from all the other descriptions and dramatically decreases the solubility of Al and N in austenite. Some limitations of TEP arise from contributions from dislocation, strain aging, and coherency strains around particles of carbon atoms in solid solution [56,58].

Some authors [14,16,59–61] have evaluated the solubility product for AlN from fundamental thermodynamic calculations, which rely on the accuracy of the latter. Wilson and Gladman [3] and Radis et al. [2] critically investigated the available data on AlN solubility products. Wilson and Gladman identify the description by Leslie et al. [19] (Nr. 2 in Table 2) as the most likely one, because of the close agreement with the experimental work of different groups, Erasmus [62], König et al. [18], and Irvine et al. [63]. Radis et al. [2] review the available AlN solubility product descriptions from the literature and rate them if AlN are clearly found in the corresponding experiments but have not been identified after annealing at higher temperatures, which is valid for the following [14,18,20] (Numbers 3,4,6 in Table 2).

Solubility data for AlN in bcc (body-centered) ferritic steel is limited, and Costa e Silva [40,41] discussed conflicting experimental results. Leslie et al. [19] found the solubility of AlN in bcc-Fe to be "vanishingly small", which was confirmed by Gladman and McIvor [69]. Iwayama and Haratani [70], for 3 % Si steel, determined the following solubility product, $\log[K] = -10062/T + 2.72$. We do not use these data in the present assessment due to their uncertainty, and we prefer to extrapolate the stability behavior of AlN from the more reliable results at higher temperatures within the austenitic steel matrix phase region.

2.4. *Previous calphad assessments*

Radis et al. [2] have proposed a Calphad-type description of AlN, which delivers a good compromise between the thermodynamic equilibrium solubility product and thermokinetics of AlN precipitation. However, they focused on a precise kinetic prediction, and their proposed thermodynamic parameters $\Delta^{\circ}H_{AlN}$ and S_{298} of the AlN phase do not agree with experimental data from the literature [31–34,53]. It should be noted that their used computation software Matcalc [71] has considerably evolved from the year of that publication, 2010, and precise thermokinetics may now be associated with a thermodynamic description with $\Delta^{\circ}H_{AlN}$ and S_{298} lying closer to literature data. Lukas [72] and Hillert and Jonsson [16] assessed the Fe-Al-N system and found a description for solid AlN with very similar thermodynamics to that tabulated by Chase (JANAF) [50]. The provided values for $\Delta^{\circ}H_{AlN}$, S_{298}, and C_{p298} of AlN further agree with the experimentally evaluated values, numbers one to ten from Table 1. Hillert and Jonsson [16] state that any modifications from available binary data for Fe-N and Fe-Al are not reasonable since these would worsen the predicted solubility of AlN in liquid and fcc-Fe. However, considering the best available data in 1992, the authors [16] anyway suggested potential improvements in the properties of the available Fe-Al system, with a remark on the solubility of Al in fcc-Fe. Sridar et al. [36] use ab initio calculations and available experimental thermochemical data for the assessment of the systems Al-N and Al-B-N. The calculated values for $\Delta^{\circ}H_{AlN}$, S_{298}, and C_{p298} of AlN from their assessed description [36] anyway better match the experimentally evaluated values from Table 1. Comparing the calculated solubility of AlN in austenite, Fig. 1, from the earliest assessed Calphad [73] description with later ones, it can be seen that consistently higher solubilities of AlN are proposed by Lukas [72], Hillert and Jonsson [16], and Thermocalc TCFE11.tdb [74]. In contrast, Sridar et al. [36] provide a remarkably lower solubility, particularly towards lower temperatures, whereas Radis et al. [2] suggest a lower solubility at high temperatures, with increasing solubility at lower temperatures, see Fig. 1.

3. Materials and sample characterization

3.1. Composition

In the present study, we use model steels within the system Fe-C-Al-N with seven compositional variations. In particular, the Al and N fractions are varied from 0.009 wt% to 0.12 wt% and 65 wt.-ppm to 86 wt.-ppm, respectively. The alloying of the material is carried out with high precision employing a vacuum induction melting furnace, followed by a casting and forging process step and homogenization annealing treatment at 1000 °C for 10 h in a vacuum furnace. The resulting concentration of the elements C, Al, Ti, Mn, and S is measured with optical emission spectroscopy (OES) and the N-fraction and O-fraction with the LECO method [25], see Table 3, providing an uncertainty of five ppm (OES) and seven ppm (LECO), respectively. The numbers in the sample labeling represent the aluminum content in 1/100 of the alloyed amount in wt.% Al, and the N content in wt.-ppm, respectively. Alloy Al1N65 from Table 3, with the lowest Al content, is used for reference measurements. In this alloy, detecting a calorimetric peak related to AlN dissolution in DSC was impossible due to its low phase fraction. The sample geometries for DSC analysis are cylindrical with Ø 1.8 mm and a height of 0.5 mm, and for EDS – particle analysis Ø 5 mm and a height of 10 mm, respectively. Computer-aided EDS particle analysis is performed on samples Al4N78, Al7N88, and Al12N86 with a similar N concentration around 80 wt ppm and varying Al.

3.2. Phase content

Fig. 2 shows the calculated pseudo-binary Fe-Al phase diagram for the composition in wt.% C = 0.5, N = 0.008, Mn = 0.12, and S = 0.0061 with the thermodynamic database TCFE11.tdb from ThermoCalc [74] and the open-licensed, most recent version of the MatCalc steel database mc_fe_v2.061.tdb [29]. The relevant precipitate phases in the austenite region are AlN and MnS. A variation in the phase boundaries for the AlN-phase is observed by comparing the orange and red lines for the descriptions from TCFE11.tdb and mc_fe_v2.061.tdb, respectively. All other phase boundaries agree well between these two database descriptions. The stars in Fig. 2 mark the experimental results for T_{solvus} of AlN for the alloys Al4N78, Al7N88, and Al12N86, see Table 6. The theoretically proposed solvus temperature for the MnS-phase is ~1240 °C (see Fig. 2) for alloys with 0.12 wt% Mn and ~1280 °C for alloys with approx. 0.2 wt% Mn. These values for T_{solvus} of MnS are also confirmed by calculations with the commercial thermodynamic database TCFE11 from Thermocalc [75], 1246 °C, and 1286 °C for the variations with high and low Mn content, respectively. T_{solvus} for AlN understandably increases with an increasing fraction of Al in the alloy.

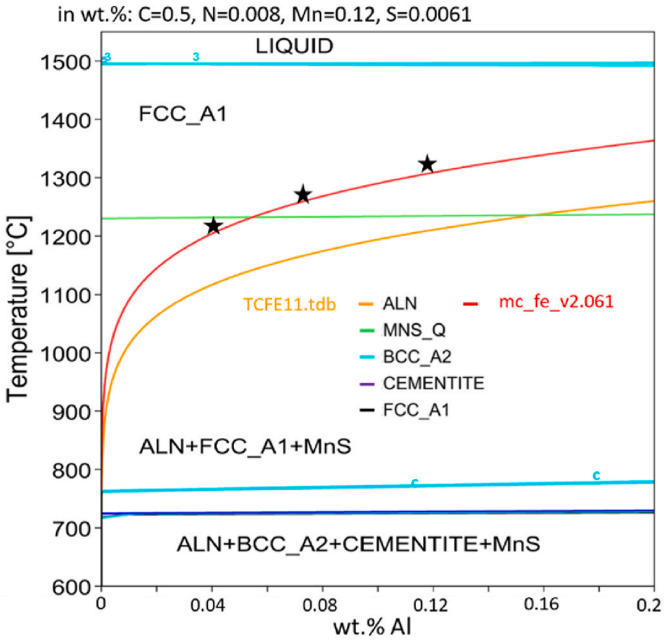

Fig. 2. Pseudo-binary Fe-Al phase diagram for the austenite region, using the thermodynamic database mc_fe_v2.061.tdb [29] and thermodynamic database TCFE11.tdb from Thermocalc [74]. The red and orange lines show the phase boundary of AlN from the descriptions of mc_fe_v2.061.tdb and TCFE11.tdb, respectively. The stars mark the experimental results for T_{solvus} of AlN for the alloys Al4N78, Al7N88, and Al12N86, respectively. (For interpretation of the references to color in this figure legend, the reader is referred to the Web version of this article.)

Note that for the alloys Al3N63, Al6N59, and Al12N65 with a lower N-fraction, the phases in the resulting pseudo-binary Fe-Al phase diagram are identical to the phases in Fig. 2; only the phase boundaries are slightly shifted in dependence of the N-fraction.

4. Methodology for the phase characterization in dilute systems

4.1. Differential scanning calorimetry

We use differential scanning calorimetry (DSC) to determine the temperatures of solid-solid phase transformations in microalloyed steel, following the approach for the evaluation of the excess heat capacity C_p developed by Milkereit et al. [26], which he presented for the case of aluminum alloys.

DSC measurements are performed on a Netzsch - STA 449 F1 Jupiter under a helium atmosphere. The measurements are carried out using corundum crucibles, with an empty crucible used as the reference sample. The device-specific heat flow can be neglected by subtracting the baseline measurement from the sample measurements. Measuring with two empty crucibles gives the baseline measurement.

Sample and baseline measurements are recorded back-to-back to avoid baseline drift problems. The measurement is done from 1000 °C to

1420 °C with a heating rate of 10 K/min. We choose the upper-temperature boundary of the DSC measurement to increase the measurement range without a change in heating rate as much as possible while still avoiding melting the material above the solidus temperature. Klimm et al. [27] state that changes in the heating rate would lead to artifacts in the heat-flux signal, which overlap with the calorimetric signal due to the dissolution of the precipitates. To allow for the maximal thermal measurement range, the theoretical solidus temperature of the material was calculated before the DSC analyses. Stepped equilibrium calculation in MatCalc [71] with the open thermodynamic database mc_fe2.061.tdb [76] developed based on the Calphad technique [73] yields a solidus temperature for the used alloys of approximately 1430 °C. Metallographic investigations of the specimen after the DSC experiment confirm that no fusing occurred during the experiment.

Dissolution and precipitation reactions are diffusional processes and are thus influenced by time and temperature. Therefore, the heating rate is an essential parameter for investigating dissolution processes. Lower heating rates broaden the peak [77] and decrease its magnitude, making it more challenging to evaluate T_{solvus} [27]. Increasing the heating rate also increases the height of the DSC peak and thus makes it easier to detect dissolution events [27]. We find that a heating rate of 10 K/min for the DSC experiments represents a good compromise between seeing distinct dissolution peaks and reaching an equilibrium state, which is a prerequisite for the use of the produced data as input for Calphad parametrizations in thermodynamic modeling.

For evaluating the accuracy of DSC results, it is notable that higher heating rates shift the endothermic peak to higher temperatures because of the necessary time for diffusion during the dissolution of the precipitates, considering the work of Osten et al. [77]. Even higher heating rates decrease the peak areas due to the more significant suppression of the diffusion processes [77]. This also means that data trend off thermodynamic equilibrium, and the lower solvus temperatures represent the values closer to the equilibrium solvus. Exemplary, we increase the heating rate to 20 K/min for alloy A12N86 to check for the influence of heating rate variations and see that it shifts the peak approximately 5 K to higher temperatures, which agrees with our expectation.

For the investigation of T_{solvus}, only the heating curve is used because of the faster dissolution than precipitation processes [27] and due to the supercooling influence on precipitation, which would shift T_{solvus} (in this case, this is the temperature of the nucleation event) to lower temperatures. Due to this imposed retardation of the precipitation event, the cooling curve can only be used as an indication that the DSC results are plausible, i.e., showing the start of AlN precipitation in a similar temperature range as its dissolution during heating.

Only the first heating step of each specimen is evaluated. Because of the long time required to form AlN [3,78], no equilibrium state during the cooling step could be reached, so a subsequent heating step with the same specimen does not give trustful results.

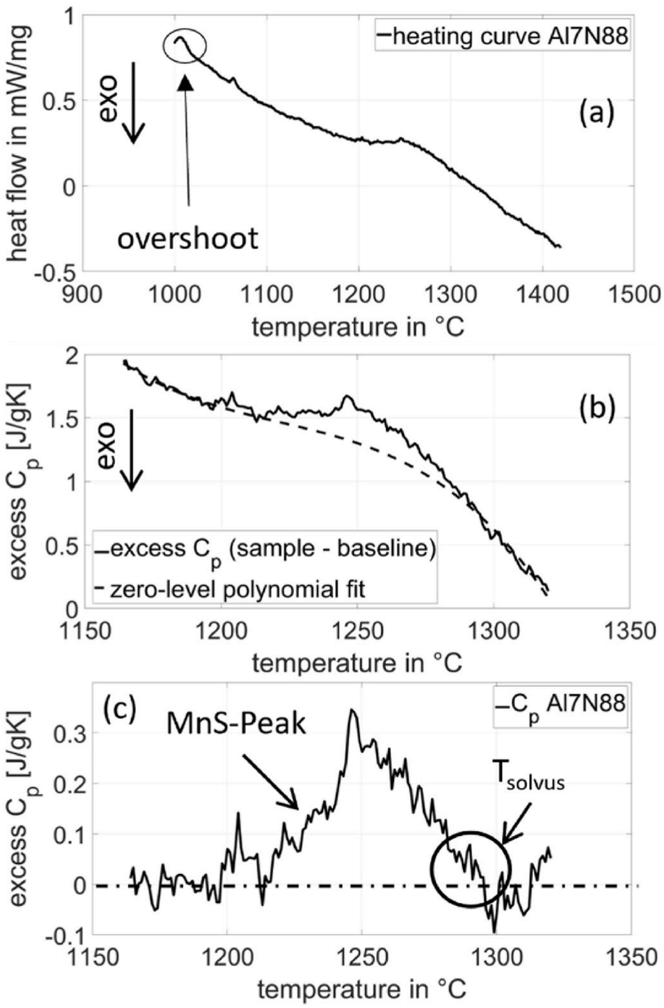

Fig. 3. Data handling to obtain an undistorted normalized DSC heating curve. Part a shows the measured heat flow. Part b gives the fitting of the zero-level polynomial at reaction-free zones. Part c gives the resulting C_p using Eq. (1).

The dissolution of precipitates corresponds to endothermic reactions, shown by deviations from the zero level. Therefore, accurate measurement and a straight- and zero-level baseline, see Fig. 3c, are necessary to distinguish between endo- and exothermic reactions and to accurately evaluate T_{solvus} of the AlN precipitates [26,77]. Milkereit et al. [26] and Osten et al. [77] state that considering the excess specific heat capacity provides advantages for the characterization of slight precipitation reactions in contrast to the heat flow curves alone because C_p allows a comparison of the heating curves concerning different heating rates and mass. For further insight, see Osten et al. [77]. Particularly in determining dissolution reactions of precipitates with low-phase fractions, any bending of the baseline needs to be minimized, and appropriate zero-level polynomials become the most important to gain accurate results [26]. Radiation losses, showing up as changes in the color of the sample, bend the baseline endothermically, and the configuration of the device influences the shape of the baseline [26,27], which is put right by subtracting the baseline from the sample measurement. In the approach by Milkereit [26], the specific heat capacity C_p is evaluated by subtracting the baseline measurement (Q_{baseline}) from the sample heat flow measurement (Q_{sample}), see Fig. 3a. The resulting C_p is normalized by division of the heat flow by the sample mass (m) and the scanning rate (β); see Eq. (1) [27],

$$C_p = \frac{\dot{Q}_{sample} - \dot{Q}_{baseline}}{m\cdot\beta} \quad . \tag{1}$$

The remaining zero-level curvature can be eliminated by subtracting a zero-level polynomial from the excess specific heat capacity (Fig. 3b). Appropriate fitting of the zero-level polynomial by carefully selecting reaction-free zones is critical for an accurate C_p curve. The zero-level polynomial must be constructed to touch the reaction-free zones asymptotically. The selection of the reaction-free zones for the parametrization of the polynomial is indeed a subjective procedure requiring much care and attention. Such zones appear as particularly smooth sections of the DSC curves. Subsequently, the resulting curve can be displayed as a function of temperature, Fig. 3c. Fig. 3c shows a small peak at approximately 1240 °C, which is most likely the dissolution peak of MnS. A potential summing up of dissolution reactions of different precipitate species in the alloy needs to be considered. That is why the high purity grade of the vacuum induction melted material and the alloying system with few elements provide a good basis for accurate DSC measurements and help generate appropriate zero-level polynomials because of broader reaction-free zones. A change in the heating rate during the experiment leads to heat-flow artifacts (overshoots), see

Fig. 3a. These overshoots need to be excluded from the evaluation.

The resulting curve for the excess heat capacity C_p is then used to evaluate the T_{solvus} of the AlN in dependence on the aluminum and nitrogen content. Fig. 4 schematically shows the correlation between the phase fraction of the dissolving phase and the DSC heat flow curve. Under equilibrium conditions, the solvus temperature of the phase coincides with C_p reaching zero level.

4.2. EDS - particle analysis

The material for PA is heat-treated in a Bähr dilatometer type 805 under a vacuum atmosphere with the annealing times and temperatures listed in Table 4. The heating and cooling rates of heat treatments are 70 K/s and 100 K/s, respectively.

With EDS – Particle Analysis, the sample is scanned and analyzed automatically within a large area around one mm^2. When the scanning electron microscope detects a particle, it finds its center, and its chemical composition is measured with EDS; the particle size and position are evaluated automatically. A precondition for the software to determine a particle as such is that at least nine measurement points (pixels) in a quadratic pattern deliver the same results. Theoretically, with a single pixel size of 10 nm, the smallest particle diameter is around 30 nm. The lower detection limit is at 60 nm when considering the actual electron beam interaction volume and the resulting origins of the X-rays. A conversion from the area of the accumulated measurement points calculates the equivalent circular diameter (ECD) of the precipitate. For the analysis, we use a JEOL JSM-7800F scanning electron microscope with a field emission gun at an operation voltage of 12 kV and an “Oxford X-MAX^{N}” - EDS detector with 50 mm^2 detector size for computer-aided EDS particle analysis (PA). A square with a side length of 1 mm is scanned. The associated area of one mm^2 is divided into 400 quadratic squares of equal size, and only every second square is measured with EDS. This allows us to check for inhomogeneities, thus seeing potential segregation zones and making it possible to investigate a more extensive area than measuring holohedral.

After finishing the PA, all the identified particles are evaluated in a subsequent step, and the AlN and MnS precipitates are determined. The first criterion to mark a particle as AlN or MnS is for ECD to be bigger than 60 nm (see above). Furthermore, the AlN-particles must contain aluminum exceeding a certain level, and – since AlN is a stoichiometric phase with negligible dissolution of other elements than Al and N – are only allowed to contain a certain fraction of carbon, manganese, sulfur, and oxygen. The exact limits for these elements are listed in Table 5. Since light elements like nitrogen cannot be detected quantitatively with EDS, nitrogen in the particle is not a condition for marking a particle as AlN. Because of the high purity of the vacuum induction melted alloy, we do not need to care about other Al-phases than AlN. Fractions of oxygen would, in fact, point to aluminum oxide, which precipitates already in the liquid or at considerably higher temperatures than AlN; thus, these particles are much bigger and much easier to detect with EDS, clearly distinguishing them from AlN. Thus, one can be sure that a particle is AlN, even if only aluminum is detected.

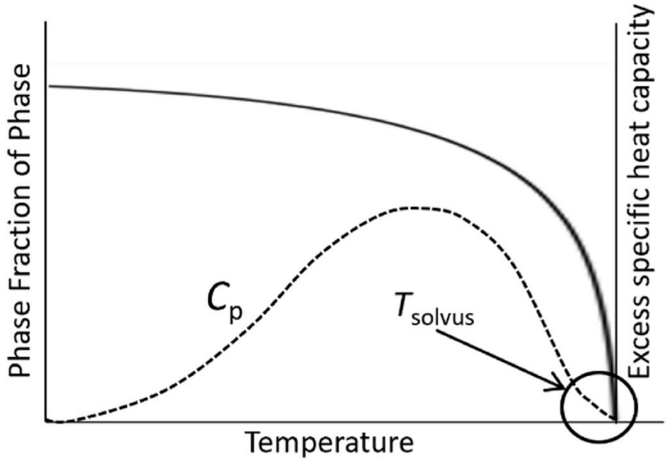

Fig. 4. Schematic correlation between phase fraction of the dissolving phase and DSC heat flow, with the position of T_{solvus} indicated.

Table 4
Parameters for the annealing heat treatment experiments before the PA examination, heating, and cooling rates for all experiments are 70K/s and 100K/s, respectively.

Nr.	annealing Temperature °C	annealing time in s	used material
1	1300	1200	Al12N86
2	1360	1200	Al12N86
3	1100	7200	Al12N86
4	1100	7200	Al7N88
5	1100	7200	Al4N78
6	1100	7200	Al1N65

Table 5
Selection limits for AlN and MnS after PA. Boundary conditions for elements are given in wt.%.

Type						
AlN	ECD >0.06 µm	Al > 2.0	C < 3.0	Mn < 0.1	S < 0.1	O < 0.1
MnS	ECD >0.06 µm	Al < 3.0	C < 3.0	Mn > 3.0	S > 0.5	O < 0.1

Table 6
Evaluated AlN - T_{solvus} of the DSC experiments for varying Al and N contents and the simulated AlN - T_{solvus}, using thermodynamic database mc_fe2.061.tdb.

Alloy	Al in wt.%	N in wt.%	exp. Tsolvus	sim. Tsolvus
Al4N78	0.038	0.0078	1220 °C	1204 °C
Al7N88	0.070	0.0088	1280 °C	1277 °C
Al12N86	0.119	0.0086	1330 °C	1333 °C
Al3N63	0.029	0.0063	1180 °C	1150 °C
Al6N59	0.060	0.0059	1240 °C	1220 °C
Al12N65	0.115	0.0065	1320 °C	1307 °C

The evaluation for MnS is similar to that for AlN. MnS, as a stochiometric phase, needs to have a certain amount of manganese and sulfur and must not exceed certain concentrations of aluminum, carbon, and oxygen, see Table 5. When all criteria are satisfied, the spatial coordinates, mean ECD, surface fraction, and precipitate size distribution of the particles are determined.

5. Results and discussion

5.1. DSC-analysis

Table 6 summarizes the results for T_{solvus} of the DSC experiments for varying Al and N contents. The evaluated T_{solvus} from Table 6 are used to calibrate the thermodynamic description of the AlN phase (see section 5.3). Conducting a DSC experiment with a 20 K/min heating rate for alloy Al12N86 results in T_{solvus} of 1340 °C, which confirms the assumption that faster heating rates shift T_{solvus} to slightly higher temperatures.

When evaluating the C_p-curves from the DSC-experiments, we find distinct peaks at ~1240 °C for the alloys with 0.12 wt% Mn, which proves the calculated T_{solvus} for MnS to be valid. Similarly, we observe peaks at 1280 °C for alloys with around 0.2 wt.-% Mn. See section 3.2 for the calculated T_{solvus} for MnS.

Using the approach described in Chapter 4.1, DSC experiments provide a powerful tool for determining the temperature of solid-solid phase transformations in diluted systems. Nevertheless, one needs to take care of the potential overlapping of dissolution peaks. Therefore, alloying systems with only a few elements are beneficial because they are more likely to avoid peak overlap and provide more extensive reaction-free zones, thus facilitating the evaluation. Furthermore, the fitting of the zero-level polynomial is, to some extent, affected by subjective construction, which in turn influences the C_p curve and can also possibly alter the evaluated dissolution temperature. The stability of AlN can be significantly influenced by the presence of impurities such as oxygen. However, using vacuum induction melting for sample preparation exceptionally lowers the impurity level (see Table 3), with oxygen levels of only some wt.-ppm. Due to the extremely low impurity levels, the influence of impurity elements on the stability of AlN is considered negligible.

5.2. *Particle analysis*

PA method to validate the DSC measurement results is used. Moreover, we get good statistical information about the distribution of precipitates (homogeneous, or heterogeneous at interfaces), particle size distribution, mean particle radii, and phase fractions. The latter is used to further evaluate the thermodynamic modeling. Moreover, the characterization of particle sizes delivers a valuable input for thermokinetic precipitation simulations within applied Calphad.

Fig. 5 shows the distribution of the AlN (blue) and MnS (red) precipitates in the specimen of alloy Al12N86 after annealing at 1100 °C for 2 h and quenching to room temperature. The precipitate size in the plot is multiplied by 100 to facilitate the visibility of precipitates. The arrangement of the precipitates in a quadratic pattern results from the applied scanning routine (see section 4.2, only every second subsquare is measured). Fig. 6 shows the AlN precipitate diameter distribution of the AlN particles depicted in Fig. 5 for alloy Al12N86 after annealing at 1100 °C for 2 h. Notably, the lower limit for detecting particles is 60 nm, so no smaller particles are visible.

The mean diameter for AlN particles is 92 nm, and the number of counted particles is 3250. The surface phase fraction is calculated by summing up the areas of all detected particles and dividing it by the total measured area. Considering the molar volumes of AlN and the matrix [79], we calculate the resulting mole fraction of AlN in the alloys. The total measured particle density is 0.00738 particles per μm^2 (approximately equivalent to $1 \cdot 10^{19}$ particles/m^3). The molar fraction for alloy Al12N86 after annealing at 1100 °C for 2 h results in $X(\mathrm{AlN}) = 9.37 \cdot 10^{-5}$. We need to consider that precipitates smaller than 60 nm in diameter cannot be detected and, thus, are not summed up in the phase fraction. This low number of particles with diameters in the detection range for SEM is the reason for the extremely difficult detection of AlN in microalloyed steel by conventional microanalytical investigation techniques. Table 7 compares the measured mole fraction of the AlN precipitates for the alloys with high N-fraction, measured with PA, and the simulated equilibrium mole fraction of AlN with the present reassessed Calphad database (see section 5.3). The measured values are always smaller than the simulated mole fractions for the AlN precipitates but within the same order of magnitude. This trend is consistent with the experimental constraint that precipitates smaller than 60 nm are not detected.

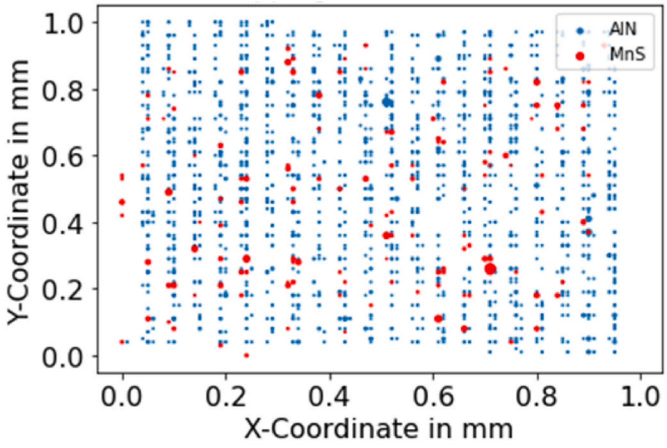

Fig. 5. Position of the AlN (blue) and MnS (red) precipitates in alloy Al12N86 after annealing at 1100 °C for 2 h, measured using the particle analysis method. The precipitate size in the plot is multiplied by 100 to make the particles easily visible. (For interpretation of the references to color in this figure legend, the reader is referred to the Web version of this article.)

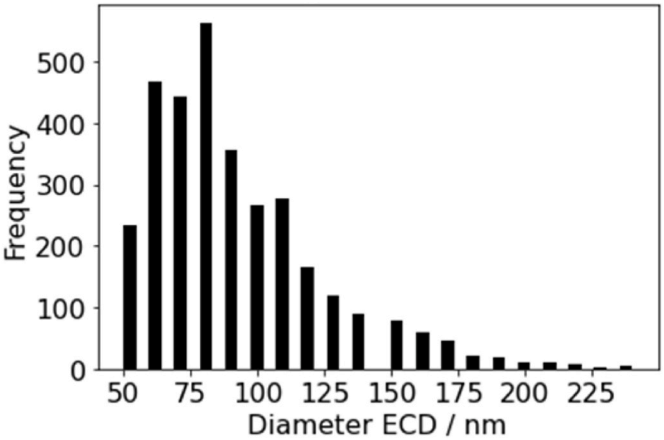

Fig. 6. Distribution of the AlN precipitates diameter in alloy Al12N86 after annealing at 1100 °C for 2 h, measurement with PA method.

For the MnS precipitates, Fig. 5, shown in red, we experimentally evaluate a mean diameter of 0.25 μm and a molar phase fraction of $1.5 \cdot 10^{-5}$. These values stay almost constant for all measurements with alloys containing 0.12 wt% Mn and 0.006 wt% S, which proves the accuracy of the measurement. The equilibrium simulation with mc_fe2.061.tdb gives a phase fraction for MnS of $2.1 \cdot 10^{-4}$, which agrees well with the experimentally evaluated results, considering the same methodological limitations as for AlN.

The results from DSC are validated by carrying out heat treatment experiments at annealing temperatures above and below T_{solvus}, exemplarily with alloy Al12N86. For parameters of the annealing treatments, see Table 4. Analyzing the resulting microstructure of the annealed specimen with PA confirms the result from the DSC measurement, whereby after annealing above T_{solvus} with 1360 °C, no AlN is found. After annealing below T_{solvus} at 1300 °C, AlN is found. We can also prove the solvus temperature for MnS to be lower than 1270 °C because of not detecting any MnS after annealing at 1270 °C.

From investigations in the SEM using wavelength dispersive spectroscopy (WDS), we can confirm a co-precipitation of AlN and MnS, see Fig. 7. The chemical mapping displays that the left part of the particle is MnS, and the right part is AlN, as stated by Lückl et al. [38]. Note that some chemical overlapping is an effect of the excitation bulb and does not indicate a solid solution among AlN and MnS.

Table 7
Comparison of the simulated and the resulting phase fraction after annealing at 1100 °C for 2 h. The simulation result is given in equilibrium mole fraction using mc_fe2.061.tdb, experimental results are evaluated with PA.

Alloy	Al in wt%	N in wt %	mole fraction simulation mc_fe2.061.tdb	mole fraction, exp. particle analysis
Al4N78	0.037	0.0078	$3.70 \cdot 10^{-4}$	$5.9 \cdot 10^{-5}$
Al7N88	0.070	0.0088	$5.77 \cdot 10^{-4}$	$1.4 \cdot 10^{-4}$
Al12N86	0.120	0.0086	$6.57 \cdot 10^{-4}$	$9.4 \cdot 10^{-5}$

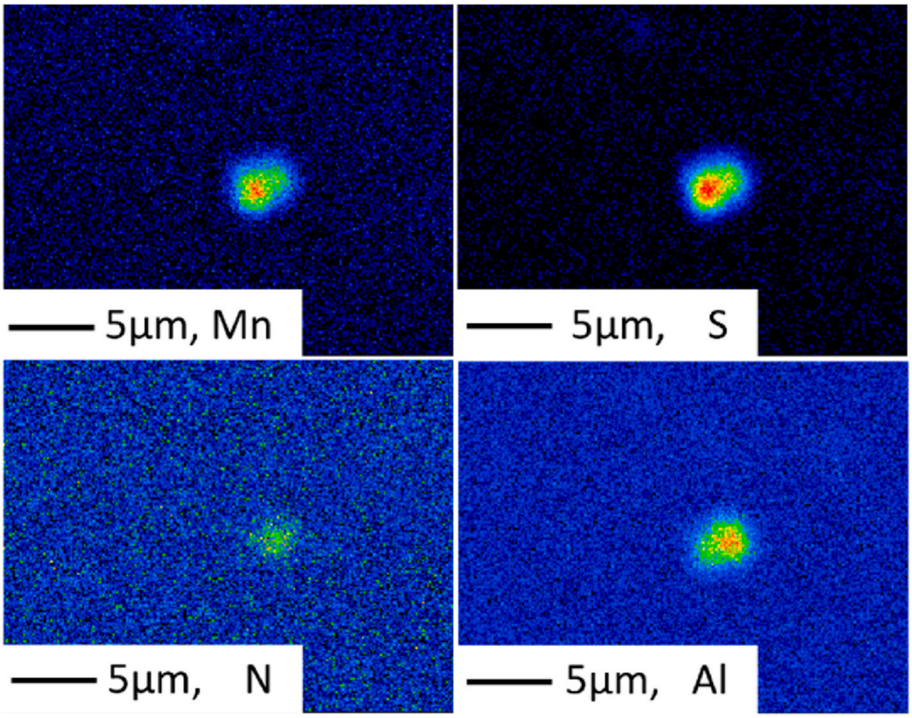

Fig. 7. Chemical mapping using WDS in alloy Al12N86 shows the co-precipitation of AlN and MnS. The mapping indicates that the left part of the particle is MnS, and the right part is AlN.

5.3. *Thermodynamic optimization of the AlN phase*

To obtain a thermodynamic description for multi-component systems, we need to be sure about appropriate thermodynamic descriptions of all lower-order systems. We adopt the descriptions of the steel matrix phases by using well-assessed existing literature descriptions listed in Table 8, and we did not find sufficiently strong arguments to reassess them. For the conceptual design of the fcc and bcc phases in the Fe-Al-N system, we follow the approach by Hillert and Jonsson [16]. The unary descriptions are taken from Dinsdale [80].

We parametrize the thermodynamic description of the AlN phase by using thermodynamic data [31–34,53] and the T_{solvus} results from DSC measurement results, considering the calorimetrically measured enthalpy of formation from numbers one to ten in Table 1, and experimental T_{solvus} results equally in the assessment. We give higher weight to experimental calorimetric data than to ab initio results because of the much more uniform results among different authors and methods for experimental $\Delta^{\circ}H_{AlN}$. We weigh the values of the standard enthalpy of formation $\Delta^{\circ}H_{AlN}$ higher than entropy and heat capacity data. The solid AlN phase is treated completely stochiometric, describing the Gibbs energy with the following expression, Eq. (2),

$$^{\circ}G_{\text{AlN}} - H^{\text{SER}} = a + bT + cTlnT + dT^2 + \frac{e}{T} + \frac{f}{T^2}. \tag{2}$$

where parameters a to f are the adjustable Calphad parameters. Parameter a is strongly controlled by the enthalpy of formation, parameter b by the entropy, and parameters c to f by the heat capacity. The polynomial terms 3 to 6 in Eq. (2), describing the heat capacity, are slightly changed from the description of Hillert and Jonsson [16], considering all input parameters of the assessment. The thermodynamic data of this reassessment is compared with previous Calphad descriptions in Table 9, showing good agreement for the enthalpy with the work of Lukas [60] and Hillert and Jonsson [16]. The calculated enthalpy of the current assessment is in best agreement with the experimentally evaluated values from Neugebauer and Margrave [34]. The deviation of the molar entropy from earlier suggestions is required in order to obtain an appropriate reproduction of the experimental DSC data on the dissolution of AlN, represented by the reassessed solubility products (see the following, chapter 5.4).

Equation (3) gives the refined Gibbs energy description for the AlN phase. The corresponding proposed modulated curve for the solubility product is dotted in purple in Fig. 9.

$$\begin{aligned} G^{AlN}_{Al:N} = & -340000 + 307 \cdot T - 48 \cdot T \cdot ln(T) - 0.0019 \cdot T^2 \\ & + 874528 \cdot T^{-1} + 1.2e^{-7} \cdot T^3. \end{aligned} \tag{3}$$

Fig. 8 compares the refined Gibbs energy description of AlN from Eq. (3) with available descriptions from thermodynamic assessments [2,16,36,60]. Concerning only G_{AlN} without considering the other relevant subsystems, Sridar et al. [36] provide up to 1600 K the most stable description. The description from Eq. (3) for G_{AlN} lies well within the available data from the literature.

Table 8
Used binary and ternary subsystems.

system	ferrite	austenite
Fe-N	Frisk [81]	Frisk [81]
Fe-C	Gustafson [82]	Gustafson [82]
Fe-Al	Seierstein [83]	Chin et al. [84]
Fe-Al-C	Chin et al. [84]	Chin et al. [84]

Table 9
Calculated values of assessed database descriptions for enthalpy $\Delta H_m{}^{\circ}$, entropy $S_{298.15}$, and heat capacity $C_{\text{p298.15}}$ for 1 mol of formula units for AlN.

Description	$H_{\text{m\_298.15}}{}^{\circ}$(J/mol)	$S_{m\_298.15}$ (J/molK)	$C_{\text{p298.15}}$ (J/K)
Radis et al. [2]	−262982	61.05	38.86
Lukas [60]	−317980	20.16	28.33
Hillert and Jonsson [16]	−318294	20.54	30.50
Sridar et al. [36]	−329146	21.40	30.81
current work	−319659	25.42	29.39

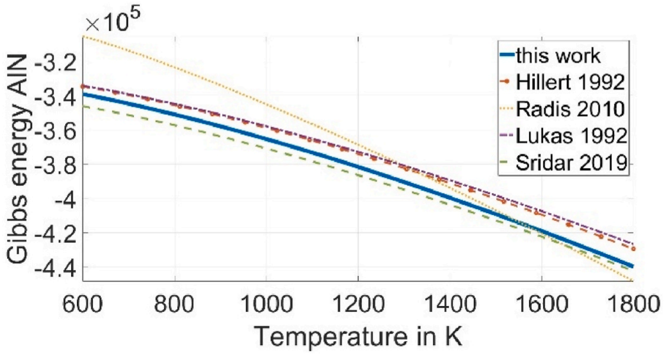

Fig. 8. Comparison of the Gibbs energy descriptions of AlN (G_{AlN}) from assessed descriptions [2,16,36,60] and this work (blue and continuous line). (For interpretation of the references to color in this figure legend, the reader is referred to the Web version of this article.)

5.4. Comparison of the solubility products

Fig. 9 shows the solubility products from the literature [14–16, 18–20,62,64,66,67], the thermodynamic database descriptions [2,16, 36,60,74], and this work, purple and dotted line in Fig. 9. For the equilibrium solubility product simulation of AlN precipitates with ThermoCalc, the commercial thermodynamic database TCFE11.tdb [74] is used. Besides the Gibbs-energy description of AlN (G_{AlN}), the descriptions of the relevant subsystems Fe-N and Fe-Al also influence the solubility product curve of the descriptions from thermodynamic databases. Lukas [60], Hillert and Jonsson [16], and Radis et al. [2] use the same descriptions for the subsystems Fe-N [83] and Fe-Al [81,83] as we are using in this work, which makes a profound comparison of the different G_{AlN} descriptions from the thermodynamic descriptions via the solubility product plot possible.

From Fig. 9, above 1450K, one can categorize the solubility products into two groups: lower-soluble AlN in austenite, as shown by lower log (K) (LS) and higher-soluble AlN (higher log(K), HS). Below 1450K, the present work results in considerably lower solubility of AlN than previously reported. This is not surprising since the higher accuracy of methods allows for decreasing the detection limits for AlN. Above 1450K, the present new data support the previously proposed LS data group.

One important aspect when finetuning the thermodynamic description for applications in dilute steel systems is carefully adapting the gradient of the resulting solubility product. Particularly at temperatures below 1400 K, the solubility product log(K) decreases below −4. For such dilute systems, it is impossible to evaluate T_{solvus} by experimental methods due to the low phase fraction, which would make it necessary to have a very high sensitivity of the experimental equipment. Nevertheless, for kinetic simulations, the stability of the AlN phase in highly diluted systems (log(K) smaller than −4) in dependence on the temperature is of great importance because it determines the temperature where a nucleation event of the precipitates can start. In the current work, we extrapolated the solubility product at lower temperatures from the experimental DSC results and assessed thermodynamic data. We confirmed the AlN stability by PA in the temperature range from 1450 K to 1600K. As a result, AlN precipitates are gradually more stable towards lower temperatures and dissolve at higher temperatures (seen by the same log(K) at higher T), compared to the description of ThermoCalc and most available literature data. Exceptions are the data by Leslie [19], lying relatively close to the present results, and Mayrhofer [20], who suggests an even lower solubility.

It is supposed that the lack of accuracy in using the Beeghly method [24], especially in not being able to detect fine precipitates, mainly led to the proposal of too high solubility products. Aside from the good reproduction of experimental dissolution temperatures of AlN with the refined Calphad description (see Table 6), the small evaluated phase fractions by PA can also be reproduced within the same order of magnitude (see Table 7).

In Fig. 10, the blue and dotted line shows our predicted solubility product compared to experimental and from thermodynamic descriptions (‘assessed’) calculated solubility products in the ferrite. All solubility descriptions show very low log(K) values, implying low solubility for Al and N in the ferrite. Experimental verification of this low solubility is difficult because concentrations are far beyond detection limits.

The solubility of AlN in ferrite is predicted by extrapolating from the austenite temperature region. Since the present thermodynamic description of the AlN phase shows good agreement with the experimental thermodynamic data and the solubility product in the austenite, and steel matrix phases are based on well-assessed subsystems, we also conclude a high accuracy for the solubility of AlN in ferrite. Good agreement of our work with the description of Lukas [60] and Hillert and Jonsson [16] is seen, which can be in part explained by the fact that

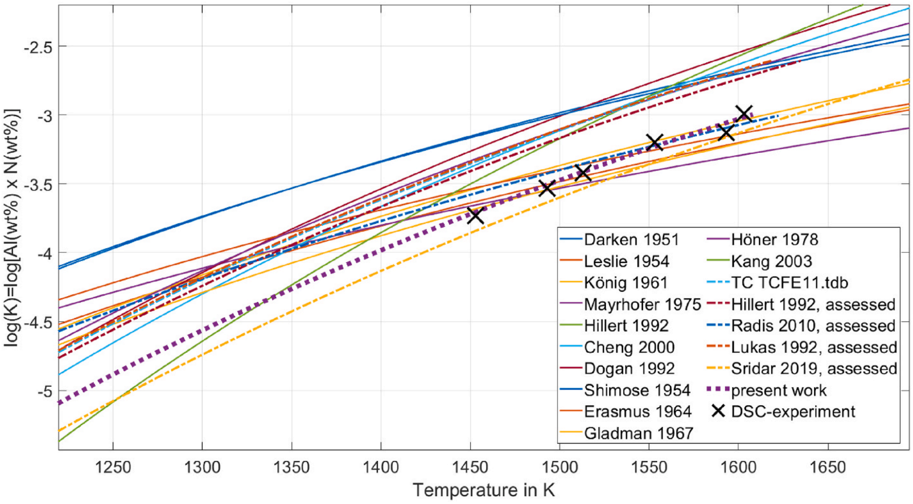

Fig. 9. Comparison of the relevant solubility products $\log(K) = \log[Al(\mathrm{wt.\%})\cdot N(\mathrm{wt.\%})]$ from the literature [14–16,18–20,62,64–67], thermodynamic descriptions from assessed descriptions [2,16,36,60,74], and the thermodynamic description from this work (purple and dotted line). ‘assessed’ accounts for evaluating the solubility product via respective thermodynamic database descriptions. (For interpretation of the references to color in this figure legend, the reader is referred to the Web version of this article.)

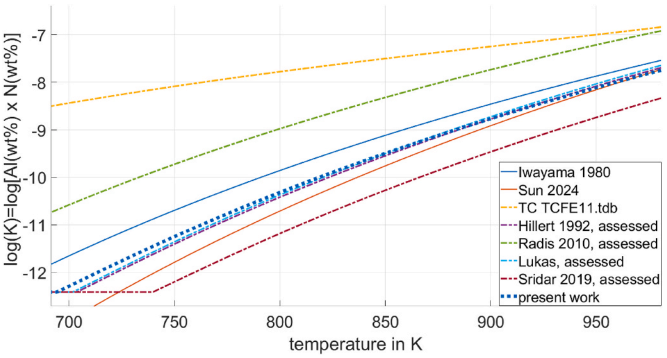

Fig. 10. Comparison of the relevant solubility products $\log(K) = \log[Al(\text{wt.\%})\cdot N(\text{wt.\%})]$ in ferrite from the literature [61,70], thermodynamic descriptions [2, 16,36,60,74], and the thermodynamic description from this work (blue and dotted line). 'assessed' accounts for evaluating the solubility product via respective thermodynamic database descriptions. (For interpretation of the references to color in this figure legend, the reader is referred to the Web version of this article.)

these authors use the same subsystems for Fe-N [83], Fe-Al [81,83], and Fe-C [82] for the steel matrix phases as in our multi-component database. In contrast, Radis et al. [2] also use the same subsystems for the matrix phase. Still, the description of G_{AlN} differs remarkably, which also explains the deviation in the solubility product result. The alteration of G_{AlN} is also seen in Fig. 8.

6. Conclusions

We successfully determined the solvus temperature of AlN in a microalloyed Fe-C-Al-N model steel by combining DSC and evaluating excess heat capacities, with EDS particle analysis. It is shown that an essential criterion for the accuracy of the evaluation of the calorimetric signals in dilute systems is the definition of appropriate zero-level polynomials. The fulfillment of this precondition is facilitated by the use of high-purity alloys with few elements.

The EDS particle analysis method is a powerful method with a high statistical significance in evaluating precipitate distribution. It mainly facilitates the investigation of precipitates with a minimum size of several tenths of nanometers with scarce heterogeneous distributions in microalloyed steel, making it possible to scan and evaluate larger areas automatically.

The new DSC and AlN phase fractions data set the base for a refined thermodynamic description of AlN. The revised expression for the Gibbs energy of AlN, giving the new experimentally evaluated stability data, together with calorimetric thermodynamic data from the literature, high weight in the Calphad assessment, indicates a lower solubility of AlN in microalloyed steel and a higher stability of AlN below 1450 K than previously proposed. Above 1450 K, the proposed $\log(K)$-T curve matches the assessed trend as proposed by the low-solubility data group. In essence, by combining results from DSC measurements and thermodynamic properties from literature for the AlN phase with assessments of the steel matrix phase from the literature for the relevant subsystems, we can accurately predict the AlN precipitation in dilute systems.

CRediT authorship contribution statement

Markus Führer: Writing – review & editing, Writing – original draft, Visualization, Validation, Software, Methodology, Investigation, Conceptualization. **Sabine Zamberger:** Writing – review & editing, Resources, Project administration, Conceptualization. **Erwin Povoden-Karadeniz:** Writing – review & editing, Resources, Project administration, Funding acquisition, Conceptualization.

Funding

This research was funded by Christian Doppler Forschungsgesellschaft in the framework of the CD-Laboratory of Interfaces and Precipitation Engineering (CDL-IPE).

Declaration of competing interest

Acknowledgments

The financial support from the Austrian Federal Ministry for Digital and Economic Affairs and the National Foundation for Research, Technology, and Development is gratefully acknowledged. The authors acknowledge Open Access Funding by TU Wien. The financial support, as well as the provision of sample material by voestalpine Forschungsservicegesellschaft Donawitz GmbH, is gratefully acknowledged by the authors. We want to thank Michael Reischl from Voestalpine Forschungsservicegesellschaft for carrying out and setting up the particle analysis measurements.

Appendix A. Supplementary data

Supplementary data to this article can be found online at https://doi.org/10.1016/j.calphad.2024.102790.

Appendix

Table 10 gives the thermodynamic Calphad [73] parameters for the phases bcc, fcc, MnS, and AlN for the system Fe-Mn-Al-C-N-S in the open-license MatCalc steel database mc_fe_v2.061.tdb [29]. The thermodynamic data for pure components is taken from Dinsdale [80], unless not shown differently in Table 9. The descriptions of the Fe-matrix phases are taken from well-established existing assessments from the literature. The Redlich-Kister-Muggianu model for the Gibbs excess energy description for the phases bcc_A2 (bcc, ferrite, α-Fe), fcc_A1(fcc, austenite, γ-Fe), MnS, and BN is used. The values refer to 1 mol of formula units and are given in SI units.

Table 10
Thermodynamic parameters for the Fe-Mn-Al-C-N-S system and the phases bcc, fcc, MnS, and AlN.

Parameter	Value	Ref.
	2 sublattice, sites: 1:3, constituents: Fe, Mn, Al, S:C, N, Va	
${}^{0}G^{bcc}_{Fe:C}$	$+322050 + 75.667\,T + \mathrm{GHSER}_{\mathrm{Fe}} + 3\cdot\mathrm{GHSER}_{\mathrm{C}}$	[82]
${}^{0}G^{bcc}_{Mn:C}$	$+10000 + 30\,T + \mathrm{GHSER}_{\mathrm{Mn}} + 3\cdot\mathrm{GHSER}_{\mathrm{C}}$	[85]

(*continued on next page*)

Table 10 (*continued*)

Parameter	Value	Ref.
${}^{0}G^{bcc}_{Al:C}$	+100000 + 80 T + GHSER$_{Al}$ + 3·GHSER$_{C}$	[84]
${}^{0}G^{bcc}_{Fe:N}$	+93562 + 165.07 T + GHSER$_{Fe}$ + 3·GHSER$_{N}$	[81]
${}^{0}G^{bcc}_{Mn:N}$	−55600 + 606.648 T - 100.41 T·LN(T) + 844897 T^{-1}	[86]
${}^{0}G^{bcc}_{Al:N}$	+23000 + 10 T + GHSER$_{Al}$ + 3·GHSER$_{N}$	[87]
${}^{0}L^{bcc}_{Fe,Al:Va}$	−122960 + 31.9888 T	[87]
${}^{1}L^{bcc}_{Fe,Al:Va}$	+3089.2	[87]
${}^{0}L^{bcc}_{Mn,Al:Va}$	−120077 + 52.851 T	[88]
${}^{1}L^{bcc}_{Mn,Al:Va}$	−40652 + 29.276 T	[88]
${}^{0}L^{bcc}_{Fe,Mn:Va}$	−2759 + 1.237 T	[89]
${}^{0}L^{bcc}_{Fe,S:Va}$	−119675–18.7201 T	[90]
${}^{0}L^{bcc}_{Fe,Mn:C}$	+34052–23.467 T	[89]
${}^{0}L^{bcc}_{Al:C,Va}$	+130000 + 14 T	[84]
${}^{0}L^{bcc}_{Fe:C,Va}$	−190 T	[82]
${}^{0}b^{bcc}_{Fe:C}$	+2.22	[82]
${}^{0}Tc^{bcc}_{Fe:C}$	+1043	[82]
FCC-Phase	2 sublattice, sites: 1:1, constituents: Fe, Mn, Al, S:C, N, Va	
${}^{0}G^{fcc}_{Fe:C}$	+77207–15.877 T + G$_{FEFCC}$ + GHSER$_{C}$	[82]
${}^{0}G^{fcc}_{Mn:C}$	+502 + 15.261 T + GHSER$_{MN}$ + GHSER$_{C}$	[89]
${}^{0}G^{fcc}_{Al:C}$	+81000 + GHSER$_{Al}$ + GHSER$_{C}$	[84]
${}^{0}G^{fcc}_{Fe:N}$	−37460 + 3 75.42 T - 37.6 T·LN(T) + GHSER$_{Fe}$ + GHSER$_{N}$	[81]
${}^{0}G^{fcc}_{Mn:N}$	−75940 + 292.226 T - 50.294 T·LN(T) + 265051 T^{-1}	[81]
${}^{0}G^{fcc}_{Al:N}$	+80 T + GHSER$_{Al}$ + GHSER$_{N}$	[86]
${}^{0}L^{fcc}_{Fe,Al:Va}$	−97000 + 26 T	This work
${}^{1}L^{fcc}_{Fe,Al:Va}$	+22600	[84]
${}^{2}L^{fcc}_{Fe,Al:Va}$	+29100 - 13 T	[84]
${}^{0}L^{fcc}_{Mn,Al:Va}$	−69300 + 25 T	[88]
${}^{1}L^{fcc}_{Mn,Al:Va}$	+8800	[88]
${}^{0}L^{fcc}_{Fe,S:Va}$	−108733 - 18 T	[90]
${}^{0}L^{fcc}_{Fe,Al:C}$	−104000 + 80 T	[84]
${}^{1}L^{fcc}_{Fe,Al:C}$	+81000	[84]
${}^{0}L^{fcc}_{Fe,Mn:C}$	+34052–23.467 T	[89]
${}^{0}L^{fcc}_{Fe,Mn:N}$	+53968–38.102 T	[86]
${}^{1}L^{fcc}_{Fe,Mn:N}$	−28787	[86]
${}^{0}L^{fcc}_{Al:C,Va}$	−80000 + 8 T	[91]
${}^{0}L^{fcc}_{Fe:C,Va}$	−34671	[82]
${}^{0}L^{fcc}_{Mn:C,Va}$	−43433	[89]
${}^{0}L^{fcc}_{Al,Mn:C,Va}$	−50000	[84]
${}^{0}L^{fcc}_{Fe:N,Va}$	−26150	[86]
${}^{0}L^{fcc}_{Mn:N,Va}$	−69698 + 11.5845 T	[86]
${}^{0}L^{fcc}_{Al,Fe,Mn:Va}$	−125000 + 45 T	This work
${}^{0}L^{fcc}_{Al,Fe,Mn:C}$	−700000 + 455 T	This work
${}^{0}b^{fcc}_{Fe:Va}$	−2.1	[92]
${}^{0}Tc^{fcc}_{Fe:Va}$	−201	[92]
${}^{0}b^{fcc}_{Fe,Mn:Va}$	0	[87]
${}^{0}Tc^{fcc}_{Fe,Mn:Va}$	−2282	[87]
${}^{1}Tc^{fcc}_{Fe,Mn:Va}$	−2068	[87]
${}^{0}b^{fcc}_{Fe:C}$	−2.1	[82]
${}^{0}Tc^{fcc}_{Fe:C}$	−201	[82]
MnS-Phase	2 sublattice, sites: 1:1, constituents: Fe, Mn: S	
${}^{0}G^{MnS}_{Fe:S}$	−70100–201.349 T + 24.2116 T ·LN(T) - 0.003402 T^{2} + GHSER$_{FE}$ + GHSER$_{S}$	[93]
${}^{0}G^{MnS}_{Mn:S}$	−182867–368.385 T + 48.2648 T ·LN(T) - 0.01153·T^{2} + GHSER$_{MN}$ + GHSER$_{S}$	[93]
${}^{0}G^{MnS}_{Fe,Mn:S}$	+8500	[93]
${}^{1}G^{MnS}_{Fe,Mn:S}$	+5500	[93]
AlN-Phase	2 sublattice, sites: 1:1, constituents: Al: N	
${}^{0}G^{AlN}_{Al:N}$	−340000 + 307 T - 48 T·LN(T) - 0.0019 T^{2} + 874528 T^{-1} + 1.2e-007 T^{3}	This work

Data availability

Data will be made available on request.

References

[1] P.R. Rios, G.S. Fonseca, Grain boundary pinning by particles, Mater. Sci. Forum 638-642 (2010) 3907–3912. https://doi.org/10.4028/www.scientific.net/MSF.638-642.3907.

[2] R. Radis, E. Kozeschnik, Kinetics of AlN precipitation in microalloyed steel, Model. Simulat. Mater. Sci. Eng. 18 (5) (2010) 55003, https://doi.org/10.1088/0965-0393/18/5/055003.

[3] F.G. Wilson, T. Gladman, Aluminium nitride in steel, Int. Mater. Rev. 33 (1) (1988) 221–286, https://doi.org/10.1179/imr.1988.33.1.221.

[4] e Silva A. Costa, Computational thermodynamics and kinetics of aluminum nitride precipitation in steel—an overview with emphasis on austenitic grain size control, J. Phase Equilib. Diffus. (2024) 1–14, https://doi.org/10.1007/s11669-024-01142-7.

[5] H.A. Wriedt, The Al−N (Aluminum-Nitrogen) system, Bulletin of Alloy Phase diagrams (4) (1986) 329–333, https://doi.org/10.1007/bf02873001.

[6] R.J. Bruls, H.T. Hintzen, G de With, et al., The temperature dependence of the Grueneisen parameters of MgSiN2, AlN, J. Phys. Chem. Solid. 62 (4) (2001) 783–792, https://doi.org/10.1016/S0022-3697(00)00258-4.

[7] X.-G. Lu, M. Selleby, B. Sundman, Assessments of molar volume and thermal expansion for selected bcc, fcc and hcp metallic elements, Calphad 29 (1) (2005) 68–89, https://doi.org/10.1016/j.calphad.2005.05.001.

[8] M. Sennour, C. Esnouf, Contribution of advanced microscopy techniques to nano-precipitates characterization: case of AlN precipitation in low-carbon steel, Acta Mater. 51 (4) (2003) 943–957, https://doi.org/10.1016/s1359-6454(02)00498-6.

[9] N. Gao, T.N. Baker, Austenite grain growth behaviour of microalloyed Al-V-N and Al-V-Ti-N steels, ISIJ Int. 38 (7) (1998) 744–751, https://doi.org/10.2355/isijinternational.38.744.

[10] Y. Chen, Y. Wang, A. Zhao, Precipitation of AlN and MnS in low carbon aluminium-killed steel, J. Iron Steel Res. Int. 19 (4) (2012) 51–56, https://doi.org/10.1016/S1006-706X(12)60087-9.

[11] V. Massardier, V. Guétaz, J. Merlin, et al., Kinetic and microstructural study of aluminium nitride precipitation in a low carbon aluminium-killed steel, Mater. Sci. Eng., A (1–2) (2003) 299–310, https://doi.org/10.1016/s0921-5093(03)00080-7.

[12] D. Lang, E. Povoden-Karadeniz, J. Schatte, et al., Thermodynamic evaluation of the Mo-rich corner of the Mo-Hf-C system including O impurities, J. Alloys Compd. 695 (2017) 372–381, https://doi.org/10.1016/j.jallcom.2016.10.227.

[13] U.R. Kattner, G. Eriksson, I. Hahn, R. Schmid-Fetzer, B. Sundman, V. Swamy, A. Kussmaul, P.J. Spencer, T.J. Anderson, T.G. Chart, E. Costa, A. Silva, B. Jansson, B.J. Lee, M. Schalin, Joint report from groups 4: use of thermodynamic software in process modelling and group 5: new applications of thermodynamic calculations, Calphad Comput. Coupling Phase Diagrams Thermochem. 24 (1) (2000) 55–94.

[14] L.M. Cheng, E.B. Hawbolt, Meadowcroft TR dissolution and coarsening oF aluminum nitride precipitates in low carbon steel — distribution, size and morphology, Can. Metall. Q. (1) (2000) 73–86, https://doi.org/10.1179/cmq.2000.39.1.73.

[15] L.S. Darken, R.P. Smith, E.W. Filer, Solubility of gaseous nitrogen in gamma iron and the effect of alloying constituents — aluminum nitride precipitation, J. Met. 3 (12) (1951) 1174–1179, https://doi.org/10.1007/bf03397430.

[16] M. Hillert, S. Jonsson, An assessment of the Al- Fe- N system, Metall Trans A 23 (11) (1992) 3141–3149, https://doi.org/10.1007/bf02646133.

[17] Y. Kang, H. Yu, J. Fu, et al., Morphology and precipitation kinetics of AlN in hot strip of low carbon steel produced by compact strip production, Mater. Sci. Eng., A 351 (1–2) (2003) 265–271, https://doi.org/10.1016/S0921-5093(02)00845-6.

[18] P. König, W. Scholz, H. Ulmer, Wechselwirkung von Aluminium, Vanadin Und Stickstoff in Aluminiumberuhigten, Mit Vanadin Und Stickstoff Legierten Schweißbaren Baustählen Mit Rd. 0,2 % C Und 1,5 % Mn, Arch. für das Eisenhuttenwes. 32 (8) (1961) 541–556, https://doi.org/10.1002/srin.196103244.

[19] W.C. Leslie, R.L. Rickett, C.L. Dotson, C.S. Watson, Solution and precipitation of aluminum nitride in relation to the structure of low carbon steels, Metallurgical Soc Amer Inst (1954) 1470–1497.

[20] M. Mayrhofer, Dissolution and separation kinetics of aluminum nitride in aluminum killed steel, BHM Berg-und Hüttenmännische Monatshefte 120 (1975) 312–321.

[21] L. Zheng, J. Lou, X. Wang, et al., Formation behavior of AlN precipitates in super-duplex stainless steel and the impact on mechanical properties, Metall. Mater. Trans. 54 (8) (2023) 3300–3310, https://doi.org/10.1007/s11661-023-07100-1.

[22] M.-K. Paek, J.-M. Jang, M. Jiang, et al., Thermodynamics of AlN formation in high manganese-aluminum alloyed liquid steels, ISIJ Int. 53 (6) (2013) 973–978, https://doi.org/10.2355/isijinternational.53.973.

[23] M.-K. Paek, J.-M. Jang, H.-J. Kang, et al., 1347-5460, Reassessment of AlN(s)=Al+ N Equilibration in Liquid Iron, vol. 53, 2013, pp. 535–537, https://doi.org/10.2355/isijinternational.53.535, 3.

[24] H.F. Beeghly, Determination of aluminum nitride nitrogen in steel, Anal. Chem. 21 (12) (1949) 1513–1519, https://doi.org/10.1021/ac60036a024.

[25] C.A. Law, Treatise of Petroleum Geology/Handbook of Petroleum Geology: Exploring for Oil and Gas Traps. Chapter 6: Evaluating Source Rocks, AAPG Special Volumes, 1999.

[26] B. Milkereit, O. Kessler, C. Schick, Precipitation and dissolution kinetics in metallic alloys with focus on aluminium alloys by calorimetry in a wide scanning rate range, Fast Scanning Calorimetry (2016) 723–773, https://doi.org/10.1007/978-3-319-31329-0_22.

[27] D. Klimm, Thermal analysis and thermodynamics, in: Materials Science, De Gruyter STEM Ser. Walter de Gruyter GmbH, 2022.

[28] JEOL USA inc. | global supplier for SEM, TEM, NMR, mass spec. https://www.jeolusa.com/, 2024. (Accessed 11 July 2024).

[29] Matcalc - solid state and kinetics precipitation. https://www.matcalc.at/index.php/databases/open-databases, 2024. (Accessed 29 July 2024).

[30] M.R. Ranade, F. Tessier, A. Navrotsky, et al., Calorimetric determination of the enthalpy of formation of InN and comparison with AlN and GaN, J. Mater. Res. 16 (10) (2001) 2824–2831, https://doi.org/10.1557/JMR.2001.0389.

[31] W.H. Dl Hildenbrand, The vaporization behavior of boron nitride and aluminum NITRIDE1, The Journal of Physical Chemistry ACS Publications (1963).

[32] A.D. Mah, E.G. King, W.W. Weller, A.U. Christensen, Thermodynamic Properties of Aluminum Nitride, US Dept. of the Interior, Bureau of Mines, 1961. Rep.Inv. 5716).

[33] J.M. McHale, A. Navrotsky, F.J. DiSalvo, Energetics of ternary nitride formation in the (Li,Ca)−(B,Al)−N system, Chem. Mater. 11 (4) (1999) 1148–1152, https://doi.org/10.1021/cm981096n.

[34] C.A. Neugebauer, J.L. Margrave, The heat of formation of aluminum nitride, Zeitschrift anorg allge chemie 290 (1–2) (1957) 82–86, https://doi.org/10.1002/zaac.19572900109.

[35] A. Zoroddu, F. Bernardini, P. Ruggerone, et al., First-principles prediction of structure, energetics, formation enthalpy, elastic constants, polarization, and piezoelectric constants of AlN, GaN, and InN: comparison of local and gradient-corrected density-functional theory, Phys. Rev. B 64 (4) (2001) 45208, https://doi.org/10.1103/PhysRevB.64.045208.

[36] S. Sridar, R. Kumar, H. Kumar, Thermodynamic modelling of Al-B-N system, Calphad 65 (2019) 291–298, https://doi.org/10.1016/j.calphad.2019.03.008.

[37] B. Mintz, J.R. Banerjee, Influence of C and Mn on hot ductility behaviour of steel and its relationship to transverse cracking in continuous casting, Mater. Sci. Technol. 26 (5) (2010) 547–551, https://doi.org/10.1179/174328409X439123.

[38] M. Lückl, T. Wojcik, E. Povoden-Karadeniz, et al., Co-Precipitation behavior of MnS and AlN in a low-carbon steel, Steel Res. 89 (3) (2018) 1700342, https://doi.org/10.1002/srin.201700342.

[39] D. Turnbull, Kinetics of heterogeneous nucleation, J. Chem. Phys. 18 (2) (1950) 198–203, https://doi.org/10.1063/1.1747588.

[40] V Costa e Silva Andre, 1, Application of Computational Modeling to the Kinetics of Precipitation of Aluminum Nitride in Steels, vol. 48, 2012, p. 471, 3.

[41] A. Costa e Silva, M.A. da Cunha, L.N.A. Viera, F. Rizzo, The thermodynamics of aluminum nitride precipitation in steels revisited, in: Poster in Calphad Conference 2011, 2011. https://calphad.org/meetings/2011/posters/p50costaesilva.pdf.

[42] F. Fichter, E. Jenny, Die Bildungswärme des Aluminiumnitrids, Helv. Chim. Acta 5 (4) (1922) 448–454, https://doi.org/10.1002/hlca.19220050406.

[43] S. Satoh, Sci. Pap. Inst. Phys. Chem. Res. 29 (1936) 19.

[44] J.H. Edgar, Properties of group III nitrides, EMIS Datareview (1994). INSPEC London, United Kingdom Series No. 11.

[45] I. Barin, Thermochemical Data of Pure Substances. 2-nd, second ed.nd ed., VCH, Weinheim, Germany, 1993.

[46] D.D. Wagman, W.H. Evans, V.B. Parker, I. Halow, S.M. Bailey, R.H. Schumm, Selected Values of Chemical Thermodynamic Properties, NBS Tech. Note 270-3, NBS, Washington, DC, 1968.

[47] O. Kubaschewski, C.B. Alcock, Metallurgical Thermodynamics, fifth ed., Permagon, Oxford, United Kingdom, 1979.

[48] O. Kubaschewski, O. Knacke, K. Hesselmann, Thermochemical Properties of Inorganic Substances, second ed., Springer Verlag Stahleisen, Berlin, 1991.

[49] V.P. Glushko, Termicheskie Konstanty Veshchestv, Tom V (VINITI, Moscow, Russia, 1971.

[50] M.W. Chase Jr., NIST-JANAF themochemical tables, fourth edition, J. Phys. Chem. (1998). Ref. Data, Monograph 9(1-1951).

[51] S. Narasimhan, S de Gironcoli, Ab initio calculation of the thermal properties of Cu: performance of the LDA and GGA, Phys. Rev. B 65 (6) (2002) 64302, https://doi.org/10.1103/PhysRevB.65.064302.

[52] B. Grabowski, T. Hickel, J. Neugebauer, Ab initio study of the thermodynamic properties of nonmagnetic elementary fcc metals: exchange-correlation-related error bars and chemical trends, Phys. Rev. B 76 (2) (2007) 24309, https://doi.org/10.1103/PhysRevB.76.024309.

[53] D. Sedmidubský, J. Leitner, P. Svoboda, et al., Heat capacity and phonon spectra of A IIIN, J. Therm. Anal. Calorim. 95 (2) (2009) 403–407, https://doi.org/10.1007/s10973-008-9246-1.

[54] A. Mucsi, Effect of hot rolled grain size on the precipitation kinetics of nitrides in low carbon Al-killed steel, J. Mater. Process. Technol. 214 (8) (2014) 1536–1545, https://doi.org/10.1016/j.jmatprotec.2014.02.024.

[55] G. Jeanmaire, M. Dehmas, A. Redjaïmia, et al., Precipitation of aluminum nitride in a high strength maraging steel with low nitrogen content, Mater. Char. 98 (2014) 193–201, https://doi.org/10.1016/j.matchar.2014.11.001.

[56] W.S. Ce Siyasiya, The effects of hot rolling process and the nitrogen and sulphur content on the microstructural development of aluminium killed hot rolled low carbon strip steel, Journal of the Southern African Institute of Mining and Metallurgy (2008).

[57] V. Massardier, N. Lavaire, M. Soler, et al., Comparison of the evaluation of the carbon content in solid solution in extra-mild steels by thermoelectric power and by internal friction, Scripta Mater. 50 (12) (2004) 1435–1439, https://doi.org/10.1016/j.scriptamat.2004.03.010.

[58] A. Brahmi, R. Borrelly, Study of aluminium nitride precipitation in pure Fe-Al-N alloy by thermoelectric power measurements, Acta Mater. 45 (5) (1997) 1889–1897, https://doi.org/10.1016/S1359-6454(96)00333-3.

[59] H. Yu, Y.L. Kang, H.B. Dong, et al., Analysis on the behavior of precipitates in ultra-thin hot strip of plain low carbon steel produced by compact strip production, acta metallurgica sinica 15 (4) (2002) 375–379.

[60] Hans Leo Lukas, Thermochemical database for light metal alloys, in: I. Ansara, A. T. Dinsdale, M.H. Rand (Eds.), System Al-N, COST507 European Communities, Luxembourg, 1998.

[61] L. Sun, P. Wang, X.-W. Lei, et al., 1543-1940, Solubility Product of Aluminum Nitride in Steels: Thermodynamic Calculations, vol. 55, 2024, pp. 2635–2643, https://doi.org/10.1007/s11661-024-07423-7, 8.

[62] La Erasmus, Effect of aluminium additions on forgeability austenite grain coarsening temperature+ impact properties of steel, Journal of the Iron and Steel (1964).

[63] K.J. Irvine, F.B. Pickering, T. Gladman, Grain-refined C-Mn Steels, vol. 202, 1967, pp. 32–41.

[64] Ö.N. Doğan, G.M. Michal, H.-W. Kwon, Pinning of austenite grain boundaries by AIN precipitates and abnormal grain growth, Metall Trans A 23 (8) (1992) 2121–2129, https://doi.org/10.1007/BF02646005.

[65] T.N.K. Shimose, Tetso-to-Hagane, J. Iron Steel Inst. Japan 40 (1954) 242.

[66] T. Gladman, Grain-coarsening of Austenite, 1967.

[67] K.E. Honer, S. Baliktay, Formation of aluminum nitride in cast steel and its influence on the susceptibility to intercrystalline fracture.–I, Giessereiforschung (30) (1978) 53–64.

[68] J. Blatt, Thermoelectric Power of Metals, Springer, New York, NY, 1976.

[69] T. Gladman, I.D. McIvor, F.B. Pickering, Some aspects of the structure-property RELATIONSHPS in high-carbon ferrite-pearlite steels, J. Iron Steel Inst. (London) (1) (1972) 247–253.

[70] K. Iwayama, T. Haratani, The dissolution and precipitation behavior of ain and MnS in grain-oriented 3% silicon-steel with high permeability, J. Magn. Magn Mater. 19 (1–3) (1980) 15–17, https://doi.org/10.1016/0304-8853(80)90540-5.

[71] E. Kozeschnik, Mean-field microstructure kinetics modeling, in: Francisca G. Caballero (Ed.), Encyclopedia of Materials: Metals and Alloys, vol. 4, 2022, pp. 521–526, https://doi.org/10.1016/b978-0-12-819726-4.00055-7.

[72] H. Wen Hl, Thermochemical database for light metal alloys, in: I. Ansara, A. T. Dinsdale, M.H. Rand (Eds.), COST507, vol. 2, European Communities, Luxembourg, 1998, pp. 65–68. Ch.

[73] L. Kaufman, H. Bernstein, Computer Calculation of Phase Diagrams. With Special Reference to Refractory Metals, Academic Press Inc, New York, 1970.

[74] Thermo-Calc Software, CALPHAD methodology - thermo-calc software. https://thermocalc.com/about-us/methodology/the-calphad-methodology/, 2023. (Accessed 5 April 2024).

[75] J.-O. Andersson, T. Helander, L. Höglund, et al., Thermo-calc & DICTRA, computational tools for materials science, Calphad 26 (2) (2002) 273–312, https://doi.org/10.1016/s0364-5916(02)00037-8.

[76] Matcalc - solid state and kinetics precipitation. https://www.matcalc.at/. (Accessed 11 August 2023).

[77] J. Osten, B. Milkereit, C. Schick, et al., Dissolution and precipitation behaviour during continuous heating of Al–Mg–Si alloys in a wide range of heating rates, Materials 8 (5) (2015) 2830–2848, https://doi.org/10.3390/ma8052830.

[78] S.E. Kang, J.R. Banerjee, A.S. Tuling, et al., Influence of B on hot ductility of high Al, TWIP steels, Mater. Sci. Eng., A 30 (4) (2014) 486–494, https://doi.org/10.1179/1743284713Y.0000000399.

[79] P. Patnaik, Handbook of Inorganic Chemicals, McGraw-Hill, 2003.

[80] A.T. Dinsdale, SGTE data for pure elements, Calphad 15 (4) (1991) 317–425, https://doi.org/10.1016/0364-5916(91)90030-n.

[81] K. Frisk, A thermodynamic evaluation of the Cr-N, Fe-N, Mo-N and Cr-Mo-N systems, Calphad 15 (1) (1991) 79–106, https://doi.org/10.1016/0364-5916(91)90028-I.

[82] P. Gustafson, A thermodynamic evaluation of the Fe-C system, Calphad (1985) 259–267.

[83] M. Seierstein, System Al–Fe. COST507, Thermochemical Database for Light Metal Alloys, vol. 2, Office for Official Publications, Luxembourg, 1998, p. 234. I. Ansara, A.T. Dinsdale, and M.H. Rand. European Commission.

[84] K.-G. Chin, H.-J. Lee, J.-H. Kwak, et al., Thermodynamic calculation on the stability of (Fe,Mn)3AlC carbide in high aluminum steels, J. Alloys Compd. 505 (1) (2010) 217–223, https://doi.org/10.1016/j.jallcom.2010.06.032.

[85] L. Huang, Y. Pan, J. Zhang, et al., Thermodynamic Assessment of the C–Nb–V Ternary System over the Whole Composition and Temperature Ranges, vol. 71, 2020 102199, https://doi.org/10.1016/j.calphad.2020.102199, 0364-5916.

[86] K. Frisk, C. Qiu, 1862-5282, A Thermodynamic Evaluation of the Solubility of N in Solid and Liquid Cr-Fe-Mn Alloys, vol. 85, 1994, pp. 60–69, https://doi.org/10.1515/ijmr-1994-850110, 1.

[87] N. Saunders, COST 507: Thermochemical Database for Light Metal Alloys, 1998.

[88] J. Miettinen, Thermodynamic Substitutional Solution Data for Steels, 1999, pp. 1–24. Report TKK-MK-76.

[89] W. Huang, Thermodynamic properties of the Fe-Mn-V-C system, Metall Trans A 22 (9) (1991) 1911–1920, https://doi.org/10.1007/BF02669859.

[90] B.-J. Lee, B. Sundman, S.I. Kim, et al., 1347-5460, Thermodynamic Calculations on the Stability of Cu2S in Low Carbon Steels, vol. 47, 2007, pp. 163–171, https://doi.org/10.2355/isijinternational.47.163, 1.

[91] J. Collins, M. Taylor, A.L. Scarlett, et al., Prior Austenite Grain Measurement: A Direct Comparison of EBSD Reconstruction, Thermal Etching and Chemical Etching, vol. 208, 2024 113656, https://doi.org/10.1016/j.matchar.2024.113656, 1044-5803.

[92] A.F. Guillermet, The Co-Fe-Ni-W-C Phase Diagram: A Thermodynamic Description and Calculated Sections for (Co-Fe-Ni) Bonded Cemented WC Tools/Das Co-Fe-Ni-W-C Zustandsdiagramm: Eine thermodynamische Beschreibung und berechnete Schnitte für Co-Fe-Ni-gebundene Hartmetall-WC-Werkzeuge, Int. J. Mater. Res. 80 (2) (1989) 83–94, https://doi.org/10.1515/ijmr-1989-800204.

[93] J. Miettinen, B. Hallstedt, 0364-5916, Thermodynamic Assessment of the Fe-FeS-MnS-Mn System, vol. 22, 1998, pp. 257–273, https://doi.org/10.1016/S0364-5916(98)00027-3, 2.